

# PIV measurements of the asymmetric wake of a two dimensional heaving hydrofoil

K. D. von Ellenrieder · S. Pothos

Received: 12 February 2007 / Revised: 25 October 2007 / Accepted: 26 October 2007 / Published online: 30 November 2007  
© Springer-Verlag 2007

**Abstract** Particle image velocimetry is used to examine the flow behind a two-dimensional heaving hydrofoil of NACA 0012 cross section, operating with heave amplitude to chord ratio of 0.215 at Strouhal numbers between 0.174 and 0.781 and a Reynolds number of 2,700. The measurements show that for Strouhal numbers larger than 0.434, the wake becomes deflected such that the average velocity profile is asymmetric about the mean heave position of the hydrofoil. The deflection angle of the wake, which is related to the average lift and drag on the hydrofoil, is found to lie between  $13^\circ$  and  $18^\circ$ . An examination of the swirl strength of the vortices generated by the hydrofoil motion reveal that the strongest vortices, which are created at the higher Strouhal numbers, dissipate most rapidly.

## Abbreviations

PIV Particle image velocimetry  
St Strouhal number  
Re Reynolds number  
CDIC Central difference image correction

---

This research article was submitted for the special issue on Animal locomotion: The hydrodynamics of swimming (Vol. 43, No. 5).

---

K. D. von Ellenrieder (✉)  
Department of Ocean Engineering, Florida Atlantic University,  
Dania Beach, FL 33004-3023, USA  
e-mail: ellenrik@seatech.fau.edu

S. Pothos  
Fluid Mechanics Research Instruments, TSI Inc,  
Shoreview, MN 55126, USA  
e-mail: stamatios.pothos@tsi.com

## 1 Introduction

An understanding of the underlying flow physics of oscillating foil propulsion is of both engineering and biological importance. From an engineering standpoint, knowledge of this type of propulsion will help to enhance the design, predictability, efficiency and control of man-made underwater vehicles. At the same time, such knowledge can be used to address fundamental biological questions about the swimming gait and bioenergetics of swimming animals, which in turn lends insight into the energetics of their locomotion and migration (Lowe 2002; Simpfendorfer and Heupel 2004). The carangiform and thunniform modes of aquatic locomotion are of special interest to engineering researchers because of their potential applications to the highly efficient propulsion of robotic underwater vehicles. In both carangiform- and thunniform-swimming modes, the driving forces are predominantly generated by the oscillatory motion of the caudal or tail fin. The front of the animal remains relatively straight and most of the thrust-generating movement is confined to the posterior 33% (carangiform) or 10% (thunniform) of its body (Barton 2007).

Since thrust production in these two modes is believed to be principally caused by lift forces acting on the tail fin, this study focuses on examining the flow structure of a two-dimensional heaving foil (e.g., airfoil/hydrofoil) in the absence of any upstream body. The vortices shed by the unsteady motion of the tail fin of an aquatic animal are part of the fluid–structure interaction that generates drag or thrust on the animal. The coupling between the fluid and foil motion is determined, in part, by the frequency of oscillation. The propulsive efficiency appears to be maximized when the non-dimensional oscillation frequency (Strouhal number) is between 0.25 and 0.35. Wake stability

analyses show that this corresponds to the frequency of the most unstable eigenmode of a jet shear layer (Triantafyllou et al. 1993). The observation that many species of fish swim with non-dimensional tail-beat frequencies near this range (Triantafyllou et al. 1991) has been taken as a nature-based corroboration of this finding.

A closely-related flow studied by Bishop and Hassan (1964), is the flow about a heaving cylinder at Reynolds numbers  $6,545 < Re < 9,660$ . As the forcing frequency of the cylinder approaches the natural Strouhal shedding frequency the fluid acts as a non-linear, self-excited oscillator. The amplitude of the lift and drag forces acting on the cylinder reach a maximum near this frequency and sharply decrease outside of a narrow frequency band. Changes in amplitude are accompanied by a corresponding change in phase. Other characteristics, typical of non-linear, self-sustained oscillators, are also exhibited including hysteresis and “frequency demultiplication”, whereby the amplitude of the lift and drag forces have local maxima at integer multiples of the natural Strouhal shedding frequency of the cylinder. Thus, as the Strouhal number was increased the cylinder passed through a series of resonance-like conditions.

In the present study, the pure heaving motion of a foil, which oscillates at zero angle of attack in a direction perpendicular to the plane of its planform, is investigated. Most previous work has tended to focus on examining the flow at Strouhal numbers that lie near the frequency corresponding to the maximum propulsive efficiency. Here, in light of the ‘frequency demultiplication effects’ identified by Bishop and Hassan (1964), a heaving hydrofoil flow is investigated over a broader range  $0.18 < St < 0.78$  at a Reynolds number of 2,700 to explore how the flow structure evolves. At low Strouhal numbers, it is found that the positions of the vortical structures in the flow are symmetrical about the mean heave line; however, for  $St > 0.434$  symmetry is lost. Previous investigations of this wake asymmetry have been conducted through particle image velocimetry (Lua et al. 2007), qualitative dye flow visualization (Jones et al. 1998) and numerical simulations (Wang 2000; Lewin and Haj-Hariri 2003). In producing thrust, the heaving hydrofoil imparts momentum to the flow. Thus, when the wake is deflected a cross-stream force component arises, so that both thrust and lift are generated. In the absence of pressure variations, the direction (sign) and magnitude of the wake deflection angle  $\varphi$  will be related to direction and magnitude of the cross-stream force  $L$  and the thrust  $T$  by the relation  $\tan \varphi = \frac{L}{T}$ . Near the hydrofoil, where pressure variations may be significant, this relation is approximate. A phenomenon related to the direction of the wake deflection angle is wake switching; Jones et al. (1998) report that the wake direction appears to change randomly during experiments, perhaps owing to small perturbations in the flow.

Here, phase-locked PIV measurements are used to experimentally determine the wake deflection angle as a function of Strouhal number, to track the motion and strength of vortices shed by the oscillating foil and to examine the velocity profile in the jet-like flow created.

## 2 Experimental apparatus and procedure

### 2.1 Experimental setup and basic parameters

The experiments were conducted in a recirculating water channel with a  $250 \times 250 \times 2,400 \text{ mm}^3$  test section (Fig. 1). The flow facility is located in the FAU Center for Hydrodynamics and Physical Oceanography and is purpose built for PIV measurements. It features glass and bottom sidewalls for optical access and a slotted rail system for rapid equipment mounting and reconfiguration. The test section is built over a  $1.22 \text{ m} \times 2.44 \text{ m}$  optical table and the entire structure is mounted on vibration-damping supports.

A hydrofoil with a symmetrical NACA0012 cross sectional profile and a chord length of  $c = 60.0 \pm 0.5 \text{ mm}$  was used for the study. The freestream velocity was  $U = 45.0 \pm 0.9 \text{ mm/s}$  giving a chord-based Reynolds number  $Re = Uc/\nu$  of  $Re = 2,700 \pm 58.5$ ; here  $\nu$  is the kinematic viscosity of water ( $\nu = 1.004 \text{ mm}^2/\text{s}$ ). The hydrofoil was mounted at an angle of attack  $\alpha = 0^\circ$ , with respect to the freestream flow direction, by clear plexiglass endplates, which were connected to a scotch yoke mechanism. The endplates produced a two-dimensional flow, by limiting three-dimensional “end effects” at the wingtips. As shown in Fig. 2, the scotch yoke, which was driven through a 10:1 gear-reducer by a servo-controlled  $\frac{1}{4}$ -HP

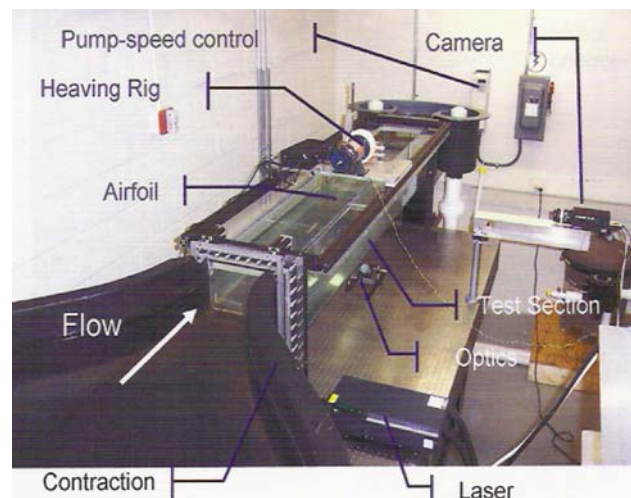
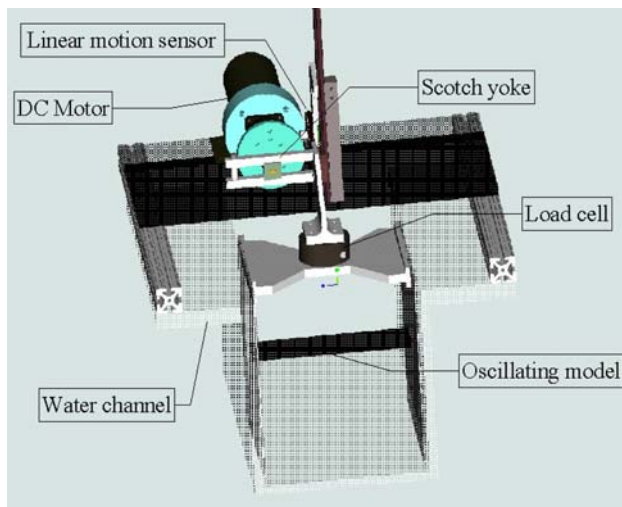


Fig. 1 Experimental setup



**Fig. 2** Heaving foil mechanism. Clear glass and plexiglass parts of test section are crosshatched

DC motor, was used to provide the sinusoidal heaving motion of the hydrofoil:

$$y(t) = y_{\max} \sin(2\pi ft) \quad (1)$$

Here,  $y(t)$  is heave position,  $y_{\max}$  is the amplitude of motion,  $t$  is time and  $f$  is the frequency of oscillation. A wheel-mounted potentiometer was used to verify the motion; a comparison of the measured heave position and a theoretical sine wave is shown in Fig. 3. The double amplitude of heaving  $2y_{\max} = A$  was  $A/c = 0.43$ . The oscillation frequency of the foil  $f$  was manually set via a servo motor controller; Strouhal number  $St \equiv fA/U$  was varied by changing the oscillation frequency of the foil while keeping both the freestream velocity and heave

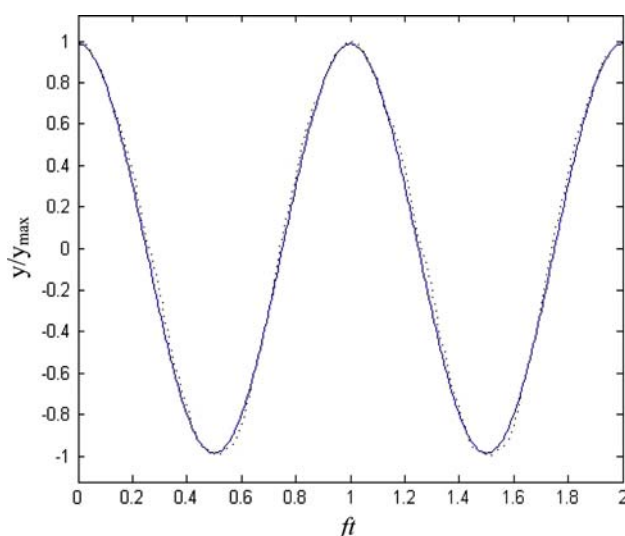


**Fig. 3** Measured (dotted line) and theoretical sine curve (solid line) heaving profile

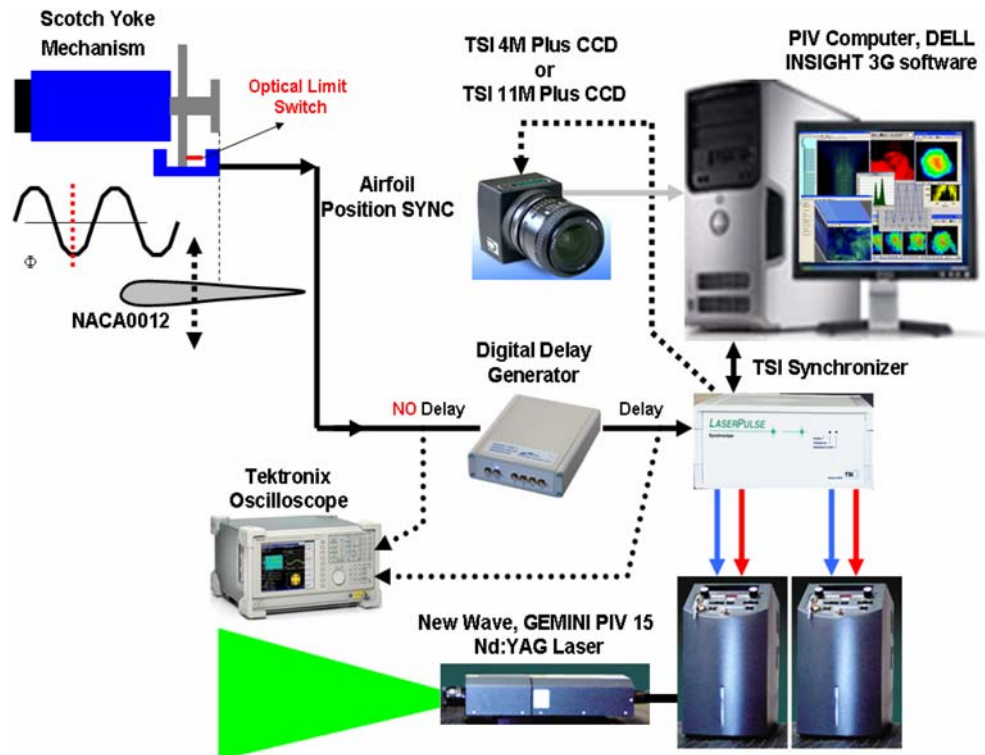
amplitude constant. Taking the uncertainties in  $f$ ,  $U$  and  $A$  into account, the range of Strouhal numbers tested was  $0.174 \pm 0.028 \leq St \leq 0.781 \pm 0.024$ . In order to compare results with other studies, the heave amplitude to chord ratio  $h = y_{\max}/c = 0.215$  and reduced frequency  $k = 2\pi cf/U$  will also be used. Note that the dimensionless quantity  $kh$  gives the ratio of maximum heave velocity to freestream speed and is related to the Strouhal number:  $kh = \pi St$ .

Image acquisition was phase-locked to the motion of the hydrofoil using an optical limit switch and a digital delay circuit (Fig. 4). The limit switch was configured such that each time the hydrofoil was at the bottom of the heave cycle a trigger pulse was sent to the digital delay generator. After an appropriate delay time the delay generator output a TTL signal that was sent to the TSI synchronizer to trigger an image acquisition sequence. By manual selection of the delay times the image capture was precisely controlled so that data were recorded at eight different phase locations separated by a phase angle of  $\Phi = 45^\circ$ , starting from the bottom of the heave motion  $y = -y_{\max}$ .

The main experimental technique used in this study was particle image velocimetry (PIV) (Adrian 1991) using high resolution commercially available CCD cameras. Two sets of data were taken (more information on each of them is provided in the Results' section). Data coming from the first set were used to determine the mean velocity and vorticity fields for  $0.174 \leq St \leq 0.781$ . In this set high-resolution PIV measurements were made using a TSI PowerView Plus  $2,048 \times 2,048$  pixel<sup>2</sup> 4 Mpixel 12-bit CCD camera. The pixel size was  $7.4 \mu\text{m}$ . A 60 mm focal length lens was used to image a  $\sim 200 \times 200$  mm<sup>2</sup> area of the flow (10.24 pixel/mm) at a magnification of  $M = 1/13.3$  and an aperture of  $f/\# 2.8$ . Data from the second set were used to determine the critical Strouhal number for the onset of the wake asymmetry within the range of  $0.260 \leq St \leq 0.607$ . In this set, high-resolution PIV measurements were made using a TSI PowerView Plus  $4,008 \times 2,672$  pixel<sup>2</sup> 11 Mpixel 12-bit CCD camera. The pixel size was  $9.0 \mu\text{m}$ . A 60-mm focal length lens was also used to image a  $\sim 355 \times 237$  mm<sup>2</sup> area of the flow (11.29 pixel/mm) at a magnification of  $M = 1/14.6$  and an aperture of  $f/\# 2.8$ .

In each experiment, the flow was seeded with 11- $\mu\text{m}$  hollow glass spheres (specific gravity of  $1.1 \text{ gm/cm}^3$ ) and a 15-Hz dual head Nd:Yag laser (New Wave Research, Gemini PIV, max power: 120 mJ/pulse, wavelength 532 nm) provided the emitted light. The two beams (exit diameter of  $\sim 5$  mm and divergence of  $\sim 4$  mrad) coming from the two laser heads were combined to travel on co-linear paths. Co-planar light sheets were formed using a combination of a set of cylindrical lenses to control the divergence of the light sheet and a spherical lens to control

**Fig. 4** Schematic of data acquisition system



the thickness of the light sheet at the measurement region. In all sets of data, two cylindrical lenses were used and the focal lengths of the lenses were  $-15$  and  $-25$  mm, respectively. At the measurement location, the thickness of the light sheet was approximately 1 mm and this was controlled by a 500-mm focal length spherical lens that was used after the combination of the aforementioned cylindrical lenses.

Both laser pulses and CCD camera frames were synchronized using a TSI synchronizer with a 1-ns resolution. The pulses from each laser head were timed to straddle neighboring CCD camera frames in order to produce images suitable for PIV cross-correlation. The time between frame-straddled laser pulses varied over the range  $2.5 \text{ ms} < \Delta t < 7.5 \text{ ms}$  depending upon the Strouhal number under investigation. High  $\Delta t$  values were used for lower Strouhal numbers while low values of  $\Delta t$  were used for higher Strouhal numbers. The main objective was to use appropriate timing between the two laser pulses that allowed for particle displacements higher than four pixels at maximum velocities.

## 2.2 PIV processing and data analysis

For each phase angle of the forcing cycle, 50 velocity fields were acquired. The vector fields were determined using TSI INSIGHT 3G PIV processing software, which implemented the central difference image correction (CDIC) deformation

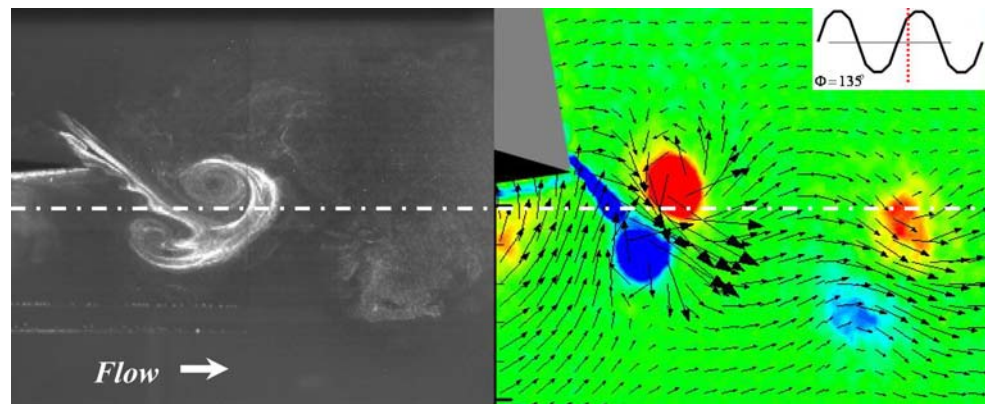
algorithm (Wereley and Gui 2003) combined with the Hart correlation (Hart 2000) method. This four-pass method employed an interrogation region of  $32 \times 32 \text{ pixel}^2$  with 75% overlap (final size). The first two passes consisted of a recursive grid to determine integer pixel displacement values while the following two passes employed the four-corner deformation grid to improve and enhance measurement accuracy. The vector fields were validated using standard velocity range criteria and a  $3 \times 3$  local median filter. Finally, any missing vectors were interpolated using a  $3 \times 3$  local mean technique; the number of spurious vectors was less than 3%. The processing algorithm maintains a spatial displacement accuracy of less than approximately 0.1 pixel, so that the spatial displacement error is on the order of less than 2.5% for a particle displacement of four pixels. The error associated with temporal variations in the laser pulse synchronization due to the jitter of the electronics is negligible since it is several orders of magnitude smaller (Adrian 1997).

## 3 Results and discussion

### 3.1 Overall flow structure

Initial flow visualization experiments using PIV seed particles as fluid tracers (Buzard 2005), revealed an asymmetric flow behind a heaving hydrofoil at  $h = 0.215$ ,  $Re = 7,000$  and  $St = 0.694$  (Fig. 5). The sequence of vortex

**Fig. 5** Asymmetric wake behind a purely heaving foil at  $St = 0.694$ ,  $h = 0.215$ ,  $\Phi = 135^\circ$ . *Left* Flow visualization,  $Re = 7,000$  (Buzard 2005). *Right* PIV velocity vector field and vorticity field,  $Re = 2,700$ . White dashed line corresponds to zero heave position,  $y/c = 0$



shedding at the trailing edge of the hydrofoil and downstream propagation for the symmetric wake is shown in Fig. 6 for  $St = 0.260$ ; the corresponding sequence for the asymmetric wake at  $St = 0.694$  is shown in Fig. 7. Each image gives the average velocity and vorticity fields at each phase position for all fifty phase-locked images. In order to capture as much of the wake as possible, the measurements were performed with the CCD camera centered at two downstream locations,  $x/c = 1$  and  $x/c = 3$ . Thus, the images shown are composites of average measurements from these two separate locations. The figures reveal the propagation of vortices past the trailing edge of the hydrofoil over one complete heaving cycle. The mean heave position is  $y/c = 0$  and the hydrofoil trailing edge is located at  $x/c = 0$ . The order of the sequence is from left to right, then top to bottom. Successive images are separated by a  $\pi/4$  phase shift in the cycle.

At  $St = 0.260$  the flow is typical of a ‘reverse von Karman vortex street’ in which two vortices are formed per cycle of oscillation (Triantafyllou et al. 2004). Lewin and Haj-Hariri (2003) report that at this Strouhal number part of the vortex shed by the leading edge of a heaving foil will be entrained into the trailing edge vortex, resulting in a weakened trailing edge vortex being deposited into the wake. This effect can be seen in Fig. 6, where the sequence of images for  $90^\circ \leq \Phi \leq 180^\circ$  shows that upstream vorticity (presumed here to be the leading edge vortex) is entrained into the trailing edge vortex as it forms.

The structure of the flow for  $St = 0.694$  is substantially different. Two vortices still form during each cycle. However, the first vortex shed pairs with the second vortex shed during the previous cycle to form a counter-rotating pair near the trailing edge of the hydrofoil. The vortex pair drifts away from the  $y/c = 0$  line to form a deflected wake.

### 3.2 Wake deflection angle

Using the averaged PIV measurements, estimates of the wake deflection angle were obtained using three separate

methods: (1) extraction of the average streamwise velocity profiles at several discrete downstream positions spanning the wake, (2) use of the centroid of swirl (rotation) at consecutively located positions over a section of the wake, and (3) use of the averaged streamwise velocity at consecutively located positions over a section of the wake.

The wake deflection angle is related to the direction and magnitude of the forces generated by the heaving hydrofoil. A control volume analysis (see Fig. 8) on the average (incompressible) steady flow with a control volume centered about the heaving hydrofoil would give:

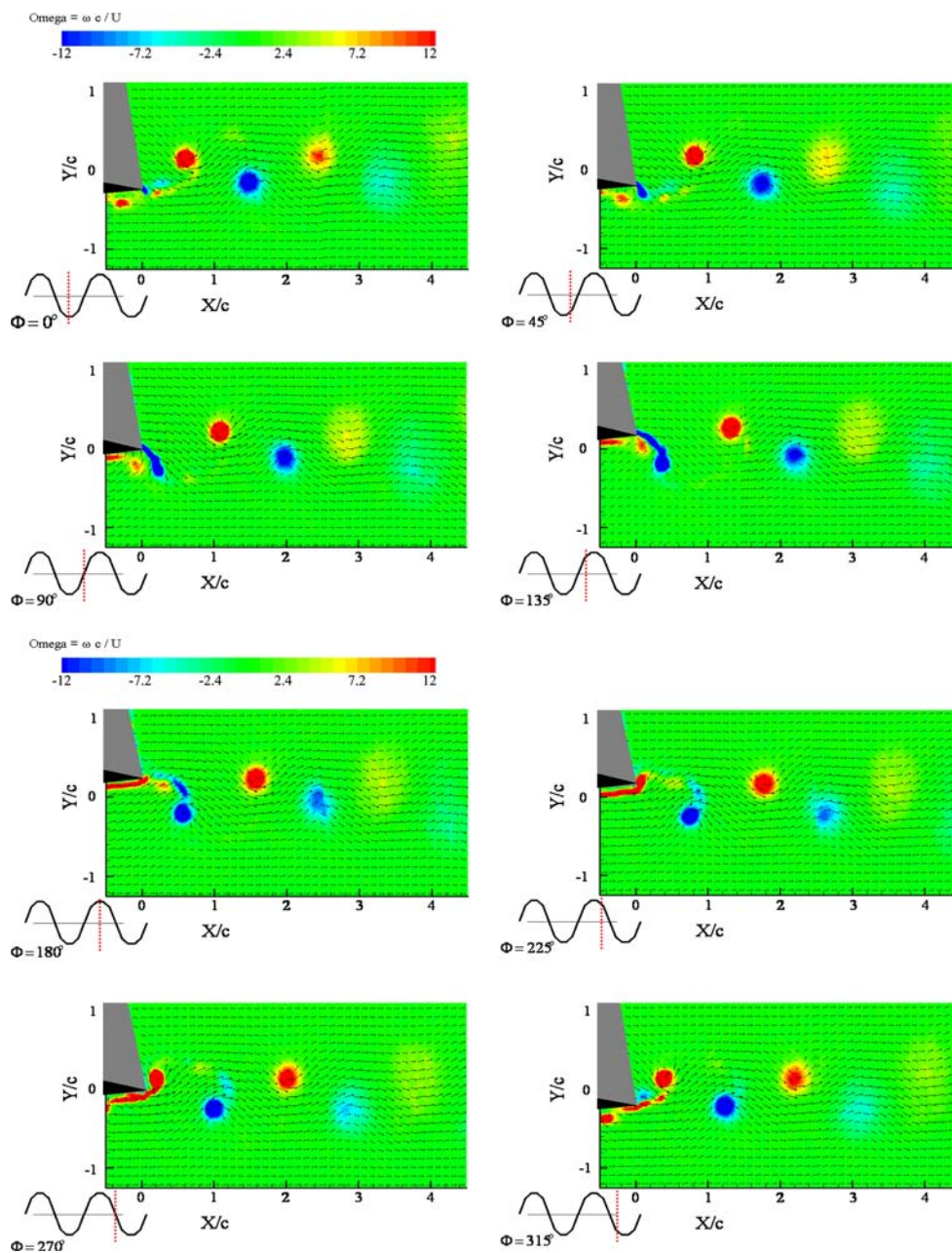
$$\iint_S \rho \vec{u} \cdot \vec{ds} = \iint_S -p \vec{ds} + \iiint_V \mu \nabla^2 \vec{u} dV + \vec{F}, \quad (2)$$

where  $\vec{F}$  is the force applied on the control volume  $V$ , which is enclosed by the surface  $S$ . If one assumes that the shear stresses arising from the viscous forces in the jet shear layer at the exit plane are negligible, then only the pressure and momentum terms will determine the direction of  $\vec{F}$ . In the experiments reported here, the measurements were performed in the vicinity of the hydrofoil, where an uneven downstream pressure distribution may affect the direction determined by a control volume analysis. Thus, the relation between the wake deflection angle and the cross-stream force  $L$  and streamwise force  $T$  is approximate:  $\tan \varphi \approx \frac{L}{T}$ .

#### 3.2.1 Wake angle from discrete downstream positions

Average velocity data were extracted from the PIV velocity vector fields for  $x/c = \{0.5, 1, 2, 3, 4\}$  chord-lengths downstream from the trailing edge of the hydrofoil. The resulting average velocity profiles reveal the tendency of the wake to become skewed from the line of mean position of the hydrofoil (i.e., to become asymmetrical about the mean position) at the higher Strouhal numbers tested. The mean velocity profiles for a symmetric wake at  $St = 0.260$  and an asymmetric wake at  $St = 0.694$ , are given in Figs. 9 and 10, respectively.

**Fig. 6** Composite PIV images centered at  $x/c = 1$  and  $x/c = 3$  for  $St = 0.260$ . Arrow length corresponds to velocity magnitude. Colored contour plots show vorticity  $\omega$  in normalized units:  $\Omega = \omega c/U$ ; positive vorticity (counter-clockwise rotation) is red, negative vorticity (clockwise rotation) is blue



In order to quantify the asymmetry, the deflection angle of the wake was calculated. As shown in Fig. 11, a linear curvefit was performed through the maximum value of  $(u - U)/U$ , where  $U$  is the freestream velocity and  $u = u(y/c)$  is the local streamwise velocity at each  $x/c$  location. The angle that the linear curvefit makes with the  $x$ -axis is the wake deflection angle. The process also permits a “wake intersection point”  $x_i$ , which is the streamwise location of the intersection of the linear curvefit and the mean heave position, to be traced back to the  $x$ -axis. The wake deflection angle and wake intersection point corresponding to each  $St$  value tested are given in Table 1.

*Wake switching:* The deflection angle for  $St = 0.520$  was not calculated using this approach because in the PIV measurements of the wake centered at  $x/c = 1$  the wake was deflected downwards, whereas in the measurements centered at  $x/c = 3$ , the wake was deflected upwards. Such switching in wake direction has been noted by Jones et al. (1998) and Lewin and Haj-Hariri (2003). Both studies report that in numerical simulations the direction appears to depend on the initial position of the hydrofoil when the heaving motion commences and that once the asymmetry develops the direction does not switch. However, Jones et al. (1998) found that the wake could switch sign somewhat randomly while a laboratory experiment was in progress,

**Fig. 7** Composite PIV images centered at  $x/c = 1$  and  $x/c = 3$  for  $St = 0.694$ . Arrow length corresponds to velocity magnitude. Colored contour plots show vorticity  $\omega$  in normalized units:  $\Omega = \omega c/U$ ; positive vorticity (counter-clockwise rotation) is red, negative vorticity (clockwise rotation) is blue

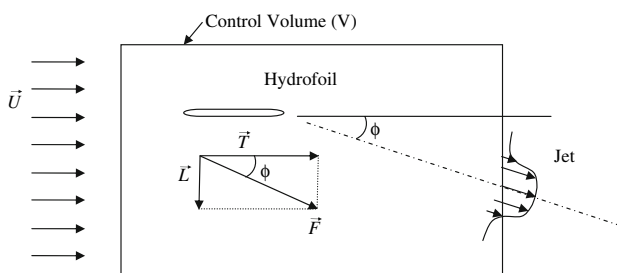
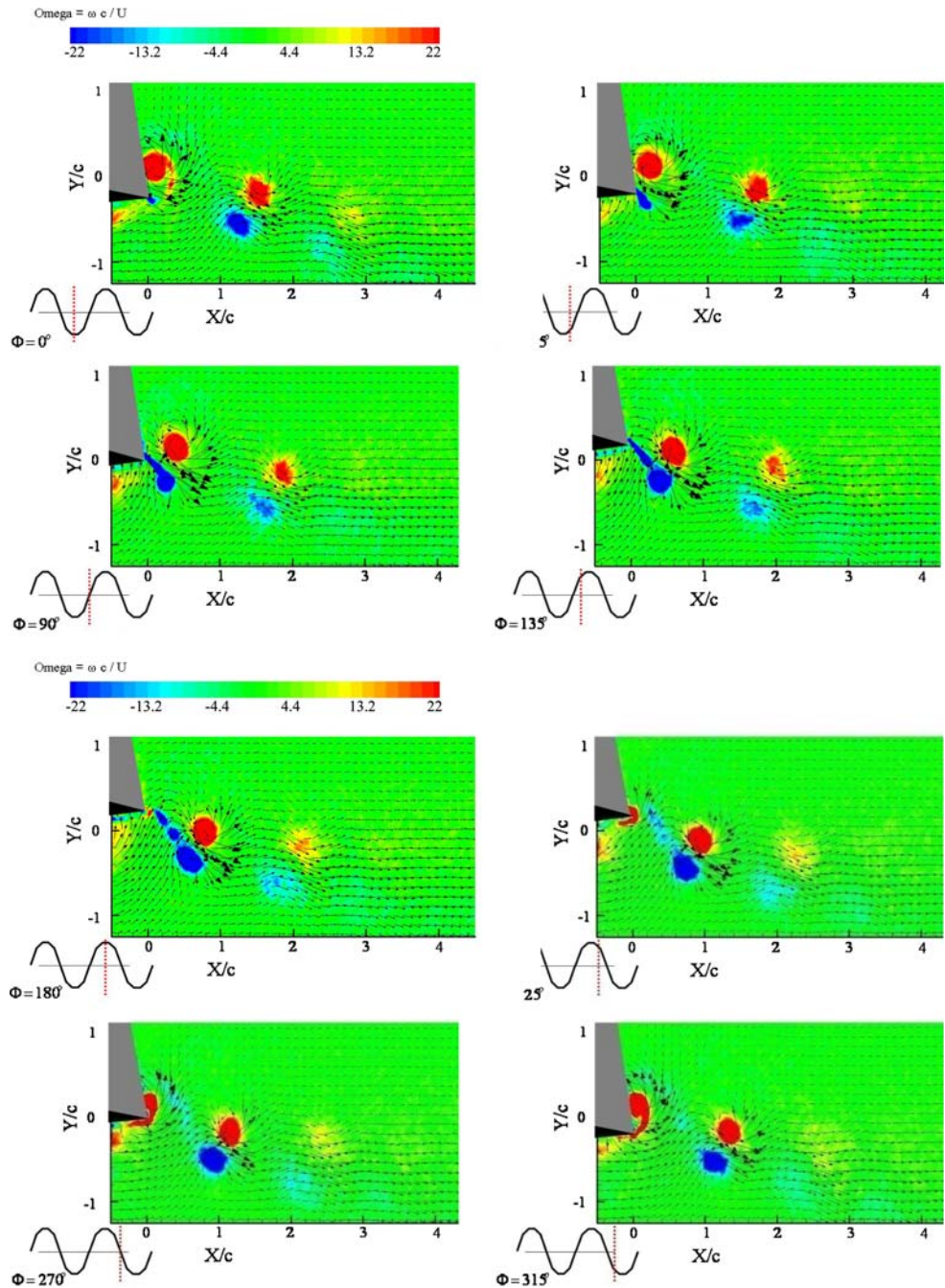


**Fig. 8** Control volume for analysis of the deflected wake

perhaps owing to the presence of disturbances. In the present study, the wake direction was only observed to switch once. This change occurred between experiments when the heaving foil mechanism was stopped and restarted, but never happened during the execution of an experiment.

### 3.2.2 Wake angle from swirl centroid

In order to further explore the wake deflection angle, and to examine the propagation of the vortices shed by the

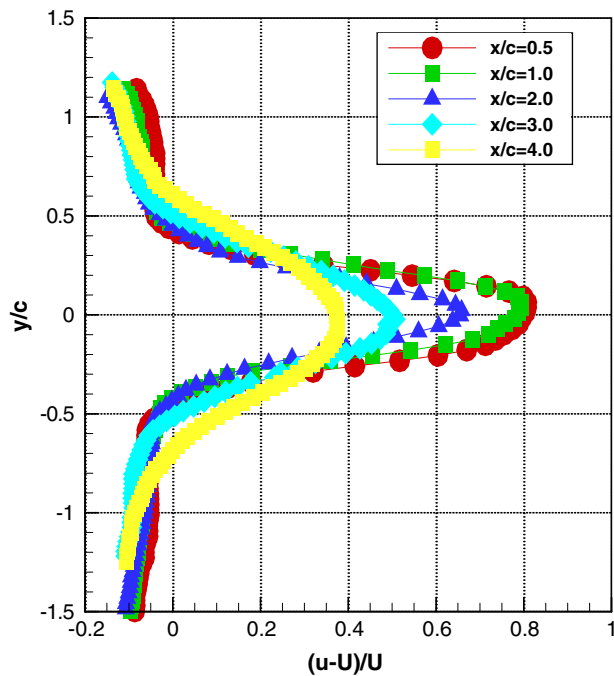


**Fig. 9** Plot of streamwise velocity profile showing symmetric wake for  $St = 0.260$

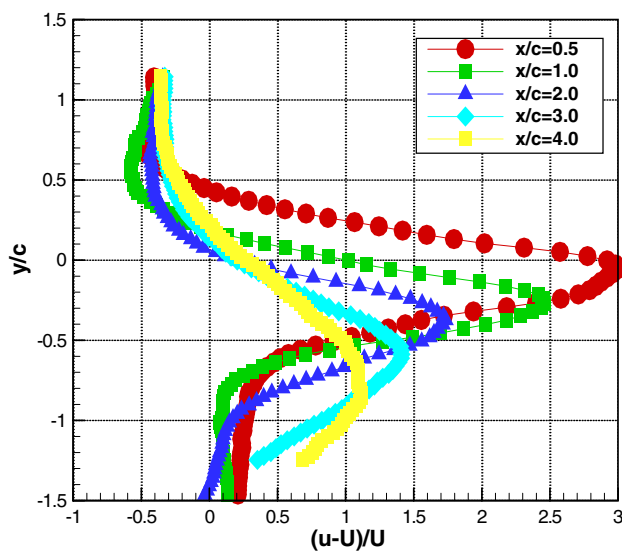


**Fig. 10** Plot of streamwise velocity profile showing asymmetric wake for  $St = 0.694$

hydrofoil, the average “swirl” and the corresponding average streamwise velocity were examined (for  $x/c = 1$ ). The two-dimensional swirl, which is normalized by the quantity  $khU/c$ , was used to identify the position and trajectory of the vortices. When the complex eigenvalues of the velocity gradient tensor are positive, particle trajectories exhibit a swirling, spiraling motion (Chong et al. 1990; Soria and Cantwell 1993). In two dimensions, the presence of the swirling fluid can be revealed by an isosurface plot

of these positive eigenvalues. The use of swirl in this case is advantageous because it distinguishes the fluid rotating about an axis from fluid rotation produced by a shear layer. Here, the swirl is computed using the techniques described in Adrian et al. (2000) and Troolin et al. (2006).

The following procedure was used to determine the wake deflection angle using swirl: (1) For each Strouhal number, the swirl was first averaged over all phases recorded. (2) For every  $x/c$  position in the averaged swirl fields, the  $y/c$  location of the swirl centroid was determined. (3) As the strongest sections of the swirl fields lie between  $0.25 \leq x/c \leq 1.5$ , least-square linear fits through the  $y/c$  centroid positions were performed over this range of  $x/c$ . (4) Using the slope and intercept of each linear fit, the angle and wake intersection point are determined (Table 2). As can be seen in Fig. 12 the use of the averaged swirl reveals the vortex trajectories over one complete cycle of the heaving motion. The curvefits are shown as dashed lines passing between rows of vortices. The wake angles determined for  $St \leq 0.434$  are less than about  $3.3^\circ$ . The onset of the asymmetry occurs within the Strouhal number range  $0.434 < St < 0.520$ , when the wake deflection angle rapidly changes by more than  $10^\circ$  and its magnitude remains between  $13^\circ \leq St \leq 18^\circ$  for  $0.520 \leq St \leq 0.781$ . At the lower Strouhal numbers the wake angle is small and the corresponding wake intersection points are located several chord lengths from the trailing edge of the hydrofoil ( $x/c = 0$ ). However, once the wake is deflected, the wake intersection point is found to be located within one third of a chord length from the position  $x/c = 0$ .

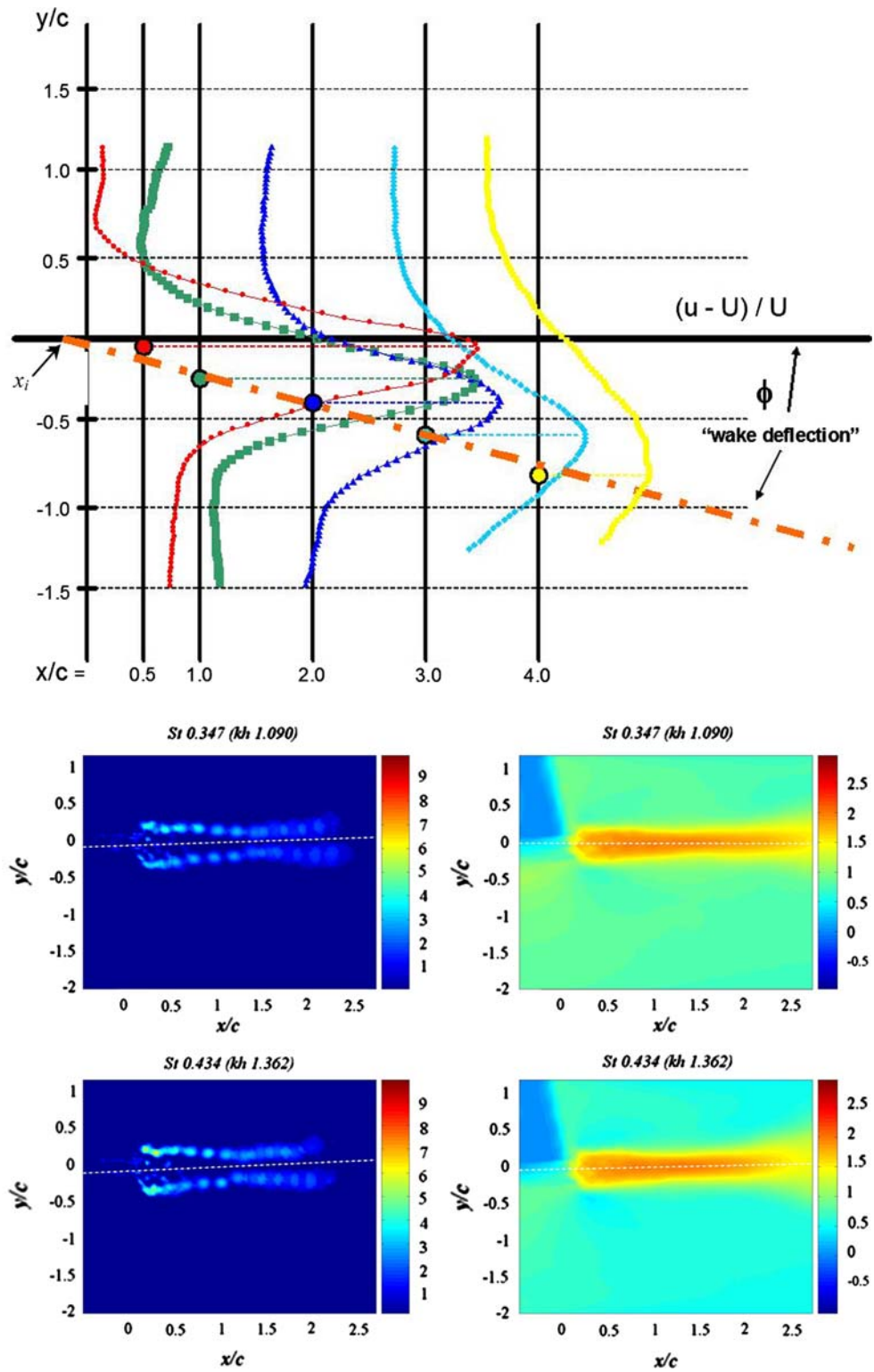
*Vortex dissipation:* In plots of swirl (normalized by  $khU$ ) centered at  $x/c = 3.0$ , it can be seen that the vortices generated at lower Strouhal numbers convect furthest downstream. As shown in Fig. 13, for  $St = 0.173$  vortices travel about four chordlengths before substantially diminishing in swirl strength. Comparatively, the vortices generated at  $St = 0.780$  only travel about 2.5 chordlengths before swirl strength vanishes. Thus, even though the vortices produced at the higher Strouhal numbers are stronger, they dissipate more rapidly. Although unclear from the measurements conducted in the present study the cause may be instability or transition to turbulence, which occurs within the rolled up shear layer of each vortex as it propagates.

### 3.2.3 Wake angle from averaged streamwise velocity at consecutively located positions

In the contour plots of swirl (Fig. 12), a slight curvature of the flow generated by the heaving hydrofoil can be seen, which is not apparent in the discretely located average



**Fig. 11** Average wake deflection angle for  $St = 0.694$ . *Left* Average Swirl, normalized by  $khU$ . *Right* Average streamwise velocity normalized by  $kh$ . In all images, *white dashed lines* correspond to linear-fits to swirl centroid (*left*) and maximum freestream velocity component (*right*) for determination of wake deflection angles. The angle between each dashed line and the  $x/c$  axis is the wake deflection angle. *Left* Average Swirl, normalized by  $khU$ . *Right* Average streamwise velocity normalized by  $kh$ . In all images, *white dashed lines* correspond to linear-fits to swirl centroid (*left*) and maximum freestream velocity component (*right*) for determination of wake deflection angles. The angle between each dashed line and the  $x/c$  axis is the wake deflection angle. *Left* Average Swirl, normalized by  $khU$ . *Right* Average streamwise velocity normalized by  $kh$ . In all images, *white dashed lines* correspond to linear-fits to swirl centroid (*left*) and maximum freestream velocity component (*right*) for determination of wake deflection angles. The angle between each dashed line and the  $x/c$  axis is the wake deflection angle.



velocity profiles (Figs. 9, 10). The wake has the appearance of a jet inclined at a shallow angle to a crossflow. To provide an additional check on the determination of the wake deflection angle, linear curvefits to the maximum streamwise velocity, averaged over all phases, for each

Strouhal number were performed. As was done for the determination of wake angles using swirl centroid, the least-square linear fits were performed for  $0.25 \leq x/c \leq 1.5$ . The slope and intercept of each linear fit was then used to determine the angle and wake intersection point

Fig. 11 continued

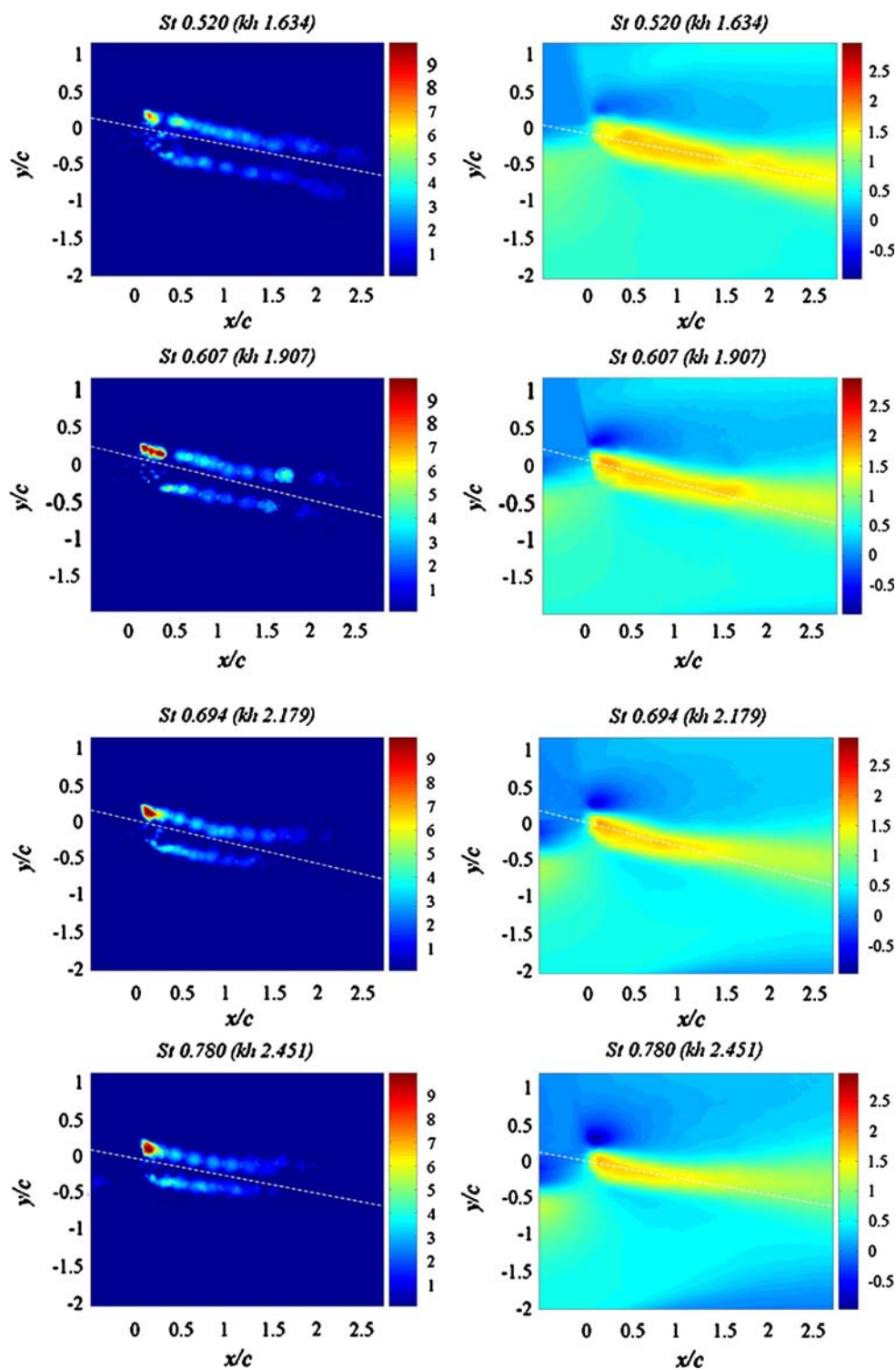


(Table 2). The curvefits are shown as dashed lines superimposed over contour plots of the average streamwise velocity in Fig. 12. The wake angles found for  $St \leq 0.434$  are much smaller than those determined using swirl and the discrete downstream location approach (see Table 3). Once again, the onset of the asymmetry occurs within the Strouhal number range  $0.434 < St < 0.520$ , when the wake

deflection angle rapidly changes by more than  $10^\circ$  and its magnitude remains between  $13^\circ < |\phi| < 18^\circ$  for  $0.520 \leq St \leq 0.781$ .

Note that from an examination of (2) above, one might also propose the use of the momentum flux (the integrand on the left-hand side of the equation) across successive downstream planes for the determination of the wake

**Table 1** Wake intersection point  $x_i/c$  and deflection angles  $\phi$  versus Strouhal number

$St$	$\phi$ ( $^\circ$ )	$x_i/c$
0.173	-0.5	-
0.260	-1.2	-
0.347	+0.8	-
0.434	+0.8	-
0.520	-	-
0.607	-9.5	-0.25
0.694	-10.7	-0.19
0.780	-7.5	-0.26

**Table 2** Wake deflection angle  $\phi$  and wake intersection point  $x_i/c$  estimated from centroid of mean swirl

$St$	$\phi$ ( $^\circ$ )	$x_i/c$
0.173	2.123	2.622
0.260	3.313	1.580
0.347	2.341	1.8553
0.434	3.157	1.6591
0.520	-13.685	0.0260
0.607	-16.937	0.3378
0.694	-16.226	0.0673
0.780	-13.350	-0.0455

deflection angle. This approach was also tested here by using the centroid of the magnitude  $|\rho\vec{u}u|$ , where  $\vec{u} = (u\vec{e}_x + v\vec{e}_y)$ . However, there was no significant difference with this approach; the results matched the wake deflection angle determined using the centroid of the maximum streamwise velocity alone to within 2%.

### 3.2.4 A comparison of the wake angle methods

As can be seen from Tables 1, 2 and 3, the three different methods employed to calculate the wake deflection angle and wake intersection points yield varying results. The greatest differences from Strouhal number to Strouhal number occur when using the discrete downstream position approach (Sect. 3.2.1). As this method utilizes relatively few downstream locations for the determination of the wake deflection, it appears to have the largest errors.

For the undeflected wake, the wake deflection angles measured using all three methods are less than approximately  $3.3^\circ$ . The maximum streamwise velocity approach (mean squared line fitting error of 3.7%) more accurately predicts the location of the undeflected wake than does the swirl centroid method (mean squared line fitting error of 7.3%). Once the wake is deflected, the deflection angles determined using the swirl centroid and maximum velocity

lie within about  $0.5^\circ$  of one another—both methods show that the deflected wake initially has an angle of about  $13^\circ$ , which increases to around  $18^\circ$  when  $0.607 \leq St \leq 0.694$ , and then decreases again to about  $13^\circ$  again with  $St = 0.780$ . Overall, the most accurate approach is the method given in Sect. 3.2.3.

### 3.3 Wake deflection onset

To determine more precisely the Strouhal number associated with the onset of the asymmetry, PIV measurements of the wake were conducted for  $0.260 \leq St \leq 0.607$ , in increments of  $\Delta St = 0.0217$ . The transition from symmetric to asymmetric wake was found to occur in the range  $0.434 < St < 0.455$ . In order to compare this finding with the previous studies, the test points have been plotted over the qualitative results presented in Fig. 2 of Lewin and Haj-Hariri (2003) (see Fig. 14). For reference, the upper bounds of the transition Strouhal number ( $1/\pi$ ) identified by Jones et al. (1998) is included. In general, it appears that the onset is dependent on both the reduced frequency  $k$  and the nondimensional heave velocity  $kh$  (not  $\pi St = kh$  alone). Note that the slope of the test points presented here gives the heave amplitude ratios  $h$ . The results the disparate studies are self-consistent in that transition is not observed for  $St < 1/\pi$ . A general trend in the data reported by Lewin and Haj-Hariri (2003) is that at higher amplitude ratios  $h$ , the wake transition appears to occur at higher nondimensional heave velocities.

### 3.4 Comparison with 3D oscillating wings

The structure of the flow behind low aspect ratio three-dimensional oscillating wings consists of continuous chains of interconnected vortex loops (von Ellenrieder et al. 2003; Blondeaux et al. 2005; Parker et al. 2005, 2007a, b; Dong et al. 2006). As the Strouhal number is increased beyond  $St \approx 0.35$  a split wake develops in which two branches of distinct interconnected vortex loops appear. This branched structure may be the three-dimensional equivalent of the deflected wake dimensional wake has the form of a bifurcated jet (Dong et al. 2006). When  $h = 0.5$ , a vertical planar cut through the two branches of interconnected vortex chains in the three-dimensional case reveals the formation of four major vortices per cycle, as seen in the two-dimensional “piston mode” case for  $h = 1$  (Triantafyllou et al. 2004). Interestingly, in the spanwise symmetry plane, the angle that the centerline of each branch of the bifurcated jet makes with the direction of the freestream flow is about  $16^\circ$ ; approximately the same as the wake deflection angle measured in the present study.

**Fig. 12** *Left* Average Swirl, normalized by  $khU$ . *Right* Average streamwise velocity normalized by  $kh$ . In all images, *white dashed lines* correspond to linear-fits to swirl centroid (*left*) and maximum freestream velocity component (*right*) for determination of wake deflection angles. The angle between each *dashed line* and the  $x/c$  axis is the wake deflection angle

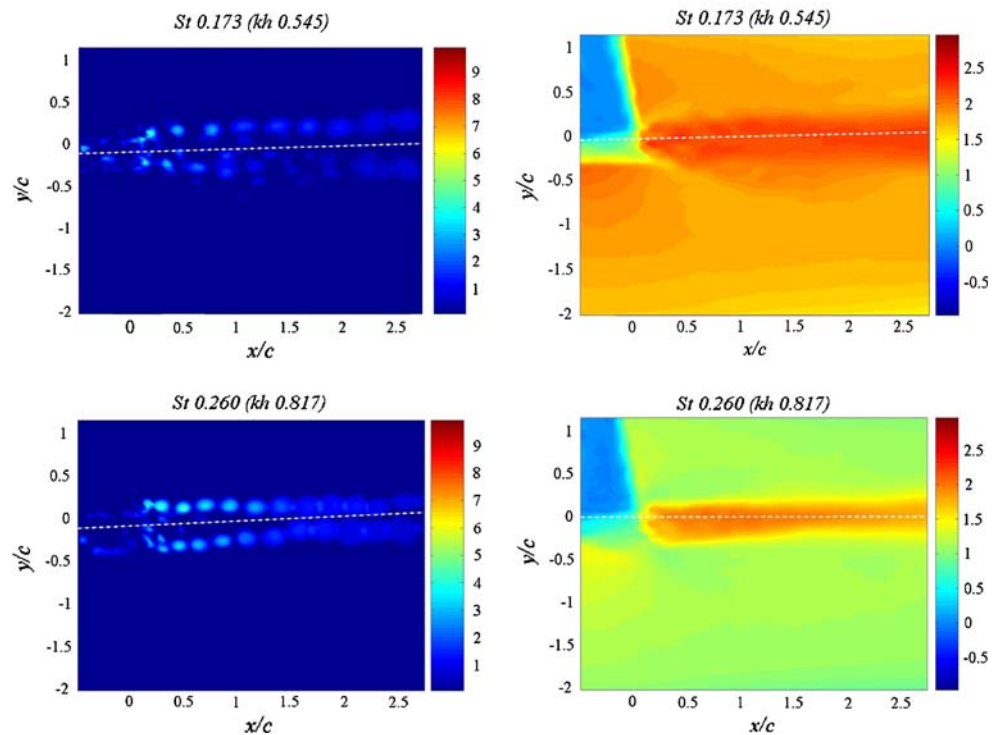
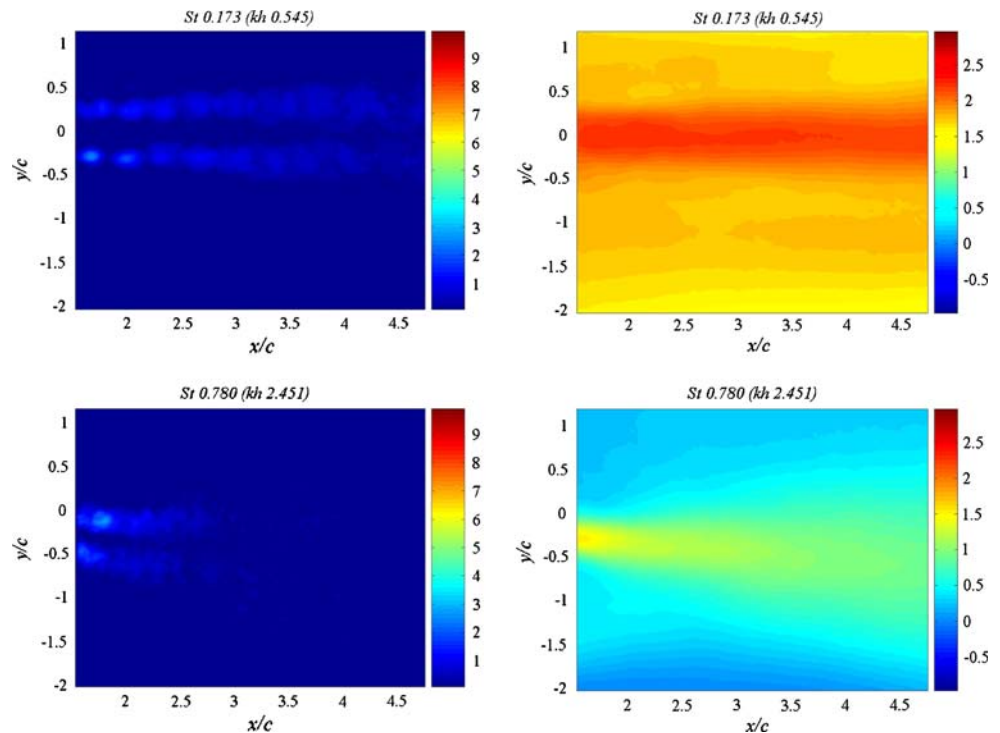


**Fig. 13** Downstream evolution of vortex flow behind heaving foil. *Left* Average Swirl, normalized by  $khU$ . *Right* Average streamwise velocity normalized by  $kh$ . Although the swirl in the vortices produced at  $St = 0.780$  is higher than in those produced at  $St = 0.173$ , the vortices dissipate more rapidly for  $St = 0.780$



#### 4 Conclusions

The experiments show that the onset of wake asymmetry for a purely heaving hydrofoil with an amplitude ratio of 0.215 will occur within the Strouhal number range  $0.434 \leq St \leq 0.455$ . As determined from both average

swirl calculations and the maxima of mean streamwise velocity, the angle of the wake deflection lies within a range of  $13^\circ \leq \varphi \leq 18^\circ$ . Consequently, the average force created by the heaving hydrofoil will have both a streamwise thrust component  $T$  and a small cross-stream lift component  $L$  with the ratio  $\tan \varphi \approx \frac{L}{T}$ . For a steadily

**Table 3** Wake deflection angle  $\phi$  and wake intersection point  $x_i/c$  estimated from maximum mean streamwise velocity

$St$	$\phi$ ( $^\circ$ )	$x_i/c$
0.173	1.597	1.044
0.260	0.108	4.441
0.347	-0.075	-34.638
0.434	1.559	2.388
0.520	-13.148	-0.298
0.607	-17.484	0.230
0.694	-17.382	0.056
0.780	-12.755	-0.097

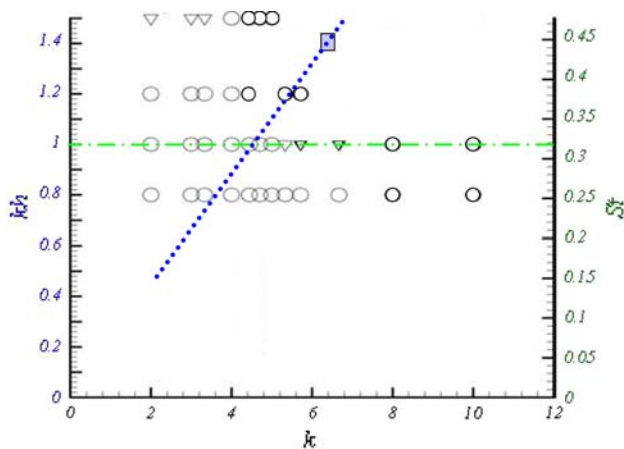


**Fig. 14** Experimental test points are plotted as reduced frequency vs. Strouhal number (*filled circle*). Values of  $k$ ,  $St$  and  $kh$  corresponding to transition from symmetric to asymmetric wake in this study are indicated by the boxed, *blue shaded region*; the flow is always asymmetric along the blue line above this *blue shaded box*. For comparison, (1) the data are superimposed on Fig. 3 of Lewin and Haj-Hariri (2003): where *circles (open square)* indicate symmetric flow, and *triangles ( $\sigma$ )* give asymmetric flow; and (2) the upper limit for wake transition ( $St \approx 1/\pi$ ) from Fig. 12 of Jones et al. (1998) is plotted (*solid line and filled square*)

heaving hydrofoil, the direction of the wake deflection is established when the heaving motion is initiated and remains the same for as long as the motion is continued. Examination of the swirl strength of the vortices shed by the heaving hydrofoil illustrates that the strongest vortices dissipate most rapidly.

**Acknowledgments** The authors thank Mr. D. R. Troolin for his valuable assistance in determining swirl from the PIV measurements.

## References

- Adrian R (1991) Particle-imaging techniques for experimental fluid mechanics. *Ann Rev Fluid Mech* 23:261–304
- Adrian R (1997) Dynamic ranges of velocity and spatial resolution of particle image velocimetry. *Meas Sci Technol* 8:1393–1398
- Adrian RJ, Christensen KT, Liu Z-C (2000) Analysis and interpretation of instantaneous turbulent velocity fields. *Exp Fluids* 29:275–290
- Barton M (2007) Bond's biology of fishes, 3rd edn. Thomson-Brooks/Cole, Belmont, CA
- Bishop RED, Hassan AY (1964) The lift and drag forces on a circular cylinder oscillating in a flowing fluid. *Proc R Soc Lond A* 277:57–75
- Blondeaux P, Fornarelli F, Guglielmini L, Triantafyllou MS, Verzicco R (2005) Numerical experiments on flapping foils mimicking fish-like locomotion. *Phys Fluids* 17:113601
- Buzard AJ (2005) Experimental study of the wake modes for propulsion of two dimensional heaving airfoils. M.S. Thesis Florida Atlantic University, Department of Ocean Engineering
- Chong MS, Perry AE, Cantwell BJ (1990) A general classification of three dimensional flow fields. *Phys Fluids A* 2:765–777
- Dong H, Mittal R, Najjar FM (2006) Wake topology and hydrodynamic performance of low aspect-ratio flapping foils. *J Fluid Mech* 566:309–343
- Hart DP (2000) PIV error correction. *Exp Fluids* 29:13–22
- Jones KD, Dohring CM, Platzer MF (1998) An experimental and computational investigation of the Knoller–Betz effect. *AIAA J* 36(7):1240–1246
- Lewin GC, Haj-Hariri H (2003) Modelling thrust generation of a two-dimensional heaving airfoil in a viscous flow. *J Fluid Mech* 492:339–362
- Lowe CG (2002) Bioenergetics of free-ranging juvenile scalloped hammerhead sharks (*Sphyrna lewini*) in Kāne'ohe Bay, O'ahu, HI. *J Exp Mar Biol Ecol* 278:141–156
- Lua KB, Lim TT, Yeo KS, Oo GY (2003) Wake-structure formation of a heaving two-dimensional elliptic airfoil. *AIAA J* 45(7):1571–1583
- Parker K, von Ellenrieder KD, Soria J (2005) Using stereo multigrad DPIV (SMDPIV) measurements to investigate the vortical skeleton behind a finite-span flapping wing. *Exp Fluids* 39:281–298
- Parker K, von Ellenrieder KD, Soria J (2007a) Morphology of the forced oscillatory flow past a finite-span wing at low Reynolds number. *J Fluid Mech* 571:327–357
- Parker K, von Ellenrieder KD, Soria J (2007b) Thrust measurements from a finite-span flapping wing. *AIAA J* 45:58–70
- Simpfendorfer CA, Heupel MR (2004) Assessing habitat use and movement. In: Carrier JC, Musick JA, Heithaus MR (eds) *Biology of sharks and their relatives*. CRC, Boca Raton, pp 553–572
- Soria J, Cantwell BJ (1993) Identification and classification of topological structures in free shear flows. In: Bonnet JP, Glauser MN (eds) *Eddy structure identification in free turbulent shear flows*. Academic, New York, pp 379–390
- Triantafyllou MS, Triantafyllou GS, Gopalkrishnan R (1991) Wake mechanics for thrust generation in oscillating foils. *Phys Fluids A* 3(12):2835–2837
- Triantafyllou MS, Triantafyllou GS, Grosenbaugh MA (1993) Optimal thrust development in oscillating foils with application to fish propulsion. *J Fluids Struct* 7:205–224
- Triantafyllou MS, Techet AH, Hover FS (2004) Review of experimental work in biomimetic foils. *IEEE J Oceanic Eng* 7:205–224
- Troolin DR, Longmire EK, Lai WT (2006) Time resolved PIV analysis of flow over a NACA0015 airfoil with Gurney flap. *Exp Fluids* 41(2):241–254
- von Ellenrieder KD, Parker K, Soria J (2003) Flow structures behind a heaving and pitching finite-span wing. *J Fluid Mech* 490:129–138
- Wang ZJ (2000) Vortex shedding and frequency selection in flapping flight. *J Fluid Mech* 410:323–341
- Wereley S, Gui L (2003) A correlation-based central difference image correction (CDIC) method and application in a four-roll mill flow PIV measurement. *Exp Fluids* 34:42–51